International Journal of Current Engineering and Technology
E-ISSN 2277 – 4106, P-ISSN 2347 – 5161

Available at http://inpressco.com/category/ijcet

Research Article

Chemically Synthesized Copper-Tin Oxide Heterojunction Photocatalysts for Hydrogen Evolution and CO_2 Methanation

[1]Maria Zaib, [1]Noor Fatima, [2]Alia Ajmal, [3]Tehreem Fatima, [4]Muhammad Nabeel Riaz and *[5]Summra Naeem

[1]Institute of Natural Sciences, Government College University Faisalabad, Pakistan
[2]Department of Chemistry, Kohat University of Science and Technology, Pakistan
[3]Department of Chemistry, National University of Sciences and Technology, Pakistan
[4]Department of Environmental Engineering, University of Agriculture Faisalabad, Pakistan
[5]Department of Environmental Sciences, University of Engineering and Technology Lahore, Pakistan

Received 01 Dec 2022, Accepted 20 Dec 2022, Available online 21 Dec 2022, **Vol.12, No.6 (Nov/Dec 2022)**

Abstract

The urgent demand for sustainable energy solutions has motivated the design of multifunctional photocatalysts that couple renewable hydrogen production with carbon utilization. In this work, copper oxide nanoparticles and copper–tin oxide heterojunction nanocomposites were synthesized through a chemical precipitation–calcination approach. Structural and optical characterization using XRD, FTIR, SEM, and UV–Vis spectroscopy confirmed the successful formation of crystalline nanostructures with strong interfacial contact and enhanced visible-light absorption. The heterojunction nanocomposites exhibited a reduced bandgap of 1.42 eV compared to 2.35 eV for pristine copper oxide, favoring improved charge excitation under solar irradiation. Photocatalytic hydrogen evolution under Xe lamp illumination reached 690 µmol g^{-1} within 10 hours, significantly higher than copper oxide alone (540 µmol g^{-1}). Systematic studies revealed optimal conditions at 45 mg catalyst loading and 70 °C, yielding up to 710 µmol g^{-1}. For CO_2 methanation, the nanocomposites achieved 96.9% conversion with 98.2% methane selectivity at 390 °C, outperforming pure copper oxide. The superior activity is attributed to efficient charge carrier separation and stable p–n heterojunction formation, as confirmed by reusability tests. These findings highlight chemically synthesized copper–tin oxide heterojunction nanocomposites as promising dual-function photocatalysts for solar-driven hydrogen generation and carbon utilization.

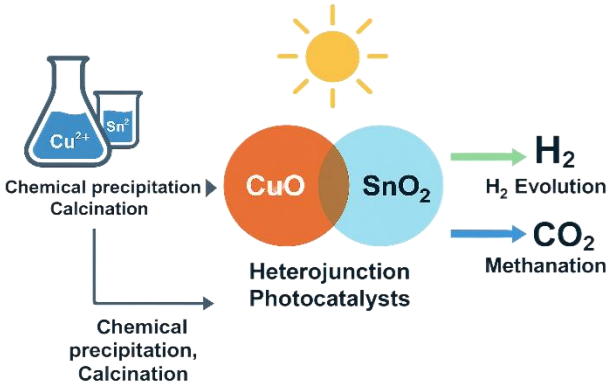

Keywords: *Copper oxide; Tin oxide, Heterojunction photocatalysts, Hydrogen evolution, CO_2 methanation, nanocomposites, Renewable energy*

1. Introduction

The global energy sector is rapidly transforming as nations seek cleaner alternatives to fossil fuels, the main drivers of greenhouse gas emissions and climate change [1]. The unprecedented consumption of coal, oil, and natural gas over the last century has led to rising atmospheric CO_2 levels, triggering global warming and associated environmental crises [2-4]. Consequently, scientists and policymakers are actively pursuing carbon-neutral energy technologies that simultaneously reduce CO_2 emissions and generate sustainable fuels [5, 6]. Among the various proposed solutions, hydrogen production through photocatalysis and CO_2 methanation stand out as two promising, complementary strategies for achieving both clean energy generation and carbon utilization [7, 8].

Hydrogen is often described as the fuel of the future due to its exceptional gravimetric energy density (120 MJ/kg) and environmentally benign combustion

*Corresponding author's ORCID ID: 0009-0003-9453-8740
DOI: https://doi.org/10.14741/ijcet/v.12.6.19

product, water vapor [9]. In comparison with conventional fossil fuels, hydrogen produces no carbon-based emissions, making it a prime candidate for powering the emerging hydrogen economy. However, the current industrial production of hydrogen relies heavily on steam reforming of natural gas, which is energy-intensive and CO_2-emitting [10, 11]. Therefore, alternative production pathways-particularly photocatalytic water splitting using semiconductor materials under solar irradiation—have attracted tremendous attention. This method not only utilizes abundant sunlight but also offers a pathway toward distributed, low-carbon hydrogen generation.

Parallel to the hydrogen challenge lies the urgent need to mitigate CO_2 accumulation in the atmosphere. One efficient approach is CO_2 methanation, in which CO_2 reacts with H_2 to produce methane (CH_4), a valuable fuel compatible with existing natural gas infrastructure [12, 13]. The Sabatier reaction, $CO_2 + 4H_2 \rightarrow CH_4 + 2H_2O$, is thermodynamically favorable at elevated temperatures in the presence of suitable catalysts [14]. By integrating hydrogen production with CO_2 methanation, a circular and sustainable energy cycle can be established: hydrogen generated by photocatalysis is used to convert CO_2 into methane, thereby closing the carbon loop while producing storable fuel [8, 15]. This dual strategy not only reduces atmospheric CO_2 levels but also provides an efficient medium for renewable energy storage and distribution.

Semiconductor nanomaterials have long been recognized as the cornerstone of photocatalysis due to their unique band structures, optical absorption, and surface reactivity [16]. Among these, copper oxide (CuO) has emerged as a highly promising candidate. CuO is a p-type semiconductor with a relatively narrow bandgap (1.2–2.0 eV), enabling visible-light absorption. It is also inexpensive, abundant, and chemically versatile, making it suitable for large-scale applications [17]. However, pristine CuO suffers from intrinsic limitations such as rapid charge recombination, photocorrosion, and limited stability under prolonged illumination [17, 18]. These drawbacks severely hinder its performance in photocatalytic hydrogen evolution and CO_2 reduction reactions.

To overcome these limitations, coupling CuO with a secondary semiconductor has proven effective in improving charge separation and extending photocatalytic activity. One of the most widely studied combinations is CuO with tin dioxide (SnO_2). SnO_2 is an n-type semiconductor with a wide bandgap (~3.6 eV), known for its high electron mobility, strong chemical stability, and compatibility with heterojunction formation [19]. When CuO and SnO_2 are integrated into a composite, they form a p–n heterojunction that promotes directional charge transfer: photoexcited electrons in the conduction band of SnO_2 can migrate efficiently, while holes in the valence band of CuO participate in oxidation reactions. This spatial separation of charge carriers suppresses recombination, enhances photocatalytic efficiency, and stabilizes the material against degradation [18].

Several studies have explored CuO–SnO_2 composites in photocatalysis, primarily targeting applications such as dye degradation and CO_2 photoreduction. For instance, coupling CuO with SnO_2 has been reported to improve photocatalytic degradation of organic dyes due to enhanced surface reactivity and charge dynamics [20]. However, fewer studies have addressed the dual application of these composites in both hydrogen production and CO_2 methanation, which is essential for creating a sustainable energy cycle. Moreover, the majority of reported works rely on either green synthesis routes using plant extracts or simple physical mixing of oxides, which may limit reproducibility, scalability, and control over interface quality.

In contrast, chemical and thermal synthesis routes offer precise control over particle size, morphology, and crystallinity, allowing systematic tuning of catalyst properties. Controlled precipitation followed by calcination is a widely adopted method that ensures homogeneity, reproducibility, and phase purity, while eliminating variability associated with plant-based synthesis [21]. Such methods are industrially relevant, as they can be scaled up with minimal modifications and without reliance on biological resources that may fluctuate in availability or composition [22]. By employing chemical synthesis, researchers can focus on tailoring interfacial properties and electronic structures rather than relying on biomolecule-mediated reduction processes.

This study reports the fabrication of copper oxide nanoparticles and copper–tin oxide nanocomposites via a controlled precipitation–calcination route, offering precise regulation of precursor concentration, pH, and calcination conditions to yield crystalline heterojunctions. Structural, optical, and morphological analyses using FTIR, XRD, SEM, and UV–Vis spectroscopy confirmed the successful formation of well-defined nanostructures. The materials were evaluated for dual catalytic functions: photocatalytic hydrogen evolution under simulated solar irradiation and thermocatalytic CO_2 methanation at elevated temperatures. The novelty of this work lies in demonstrating a scalable chemical synthesis method, assessing multifunctionality in two complementary applications, and providing mechanistic insights into charge carrier dynamics and reaction pathways. Overall, the copper–tin oxide nanocomposites exhibited superior performance compared with pure copper oxide, underscoring their promise as versatile catalysts for sustainable hydrogen production and carbon utilization.

2. Materials and Methods

2.1 Chemicals and Precursors

All chemical reagents used in this study were of analytical grade and were employed without further purification. Copper(II) chloride dihydrate ($CuCl_2 \cdot 2H_2O$, 99%), tin(II) chloride dihydrate ($SnCl_2 \cdot 2H_2O$, 98%), sodium hydroxide pellets (NaOH,

99%), methanol (CH_3OH, 99%), and high-purity carbon dioxide gas (99.99%) were purchased from J K Enterprises. Distilled and deionized water was used throughout the experiments for solution preparation and washing. The choice of these precursors was based on their solubility, stability, and compatibility with precipitation–calcination synthesis routes.

2.2 Synthesis of CuO Nanoparticles

CuO nanoparticles were synthesized using a controlled precipitation method followed by thermal calcination. Initially, 0.25 M aqueous $CuCl_2{\cdot}2H_2O$ solution was prepared by dissolving the required amount of salt in 200 mL of distilled water under constant stirring at room temperature. A 1.0 M NaOH solution was then added dropwise at a rate of 2 mL/min until the pH of the mixture reached approximately 11. The addition of NaOH resulted in the gradual precipitation of light-blue $Cu(OH)_2$. The suspension was stirred vigorously for 2 hours to ensure complete precipitation and nucleation. The product was then aged for an additional 12 hours at ambient temperature to enhance particle homogeneity. The precipitate was separated by centrifugation at 5000 rpm for 10 minutes, repeatedly washed with distilled water until neutral pH was achieved, and finally rinsed with ethanol to remove residual chloride ions. The washed precipitate was oven-dried at 90 °C for 10 hours, followed by calcination in a muffle furnace at 500 °C for 3.5 hours under air. This treatment converted $Cu(OH)_2$ into black crystalline CuO nanoparticles. The yield was approximately 1.8 g from the batch synthesis, with particle size controlled by calcination temperature and precursor concentration.

2.3 Fabrication of CuO@SnO_2 Nanocomposites

To synthesize the CuO@SnO_2 nanocomposites, 1 g of as-prepared CuO nanoparticles was dispersed in 100 mL of deionized water and ultrasonicated for 20 minutes to achieve a uniform suspension. Separately, 0.6 g of $SnCl_2{\cdot}2H_2O$ was dissolved in 50 mL of distilled water under mild stirring to form a clear precursor solution. The $SnCl_2$ solution was then added dropwise into the CuO suspension under constant stirring at 70 °C. After 2 hours of reaction, NaOH solution (0.5 M) was added slowly to adjust the pH to 9, facilitating the hydrolysis of Sn^{2+} and deposition of $Sn(OH)_2$ on the CuO surface. The resulting mixture was aged at 70 °C for an additional hour. The precipitate was recovered by centrifugation, washed repeatedly with deionized water and ethanol, and dried at 100 °C for 8 hours. The dried powder was finally calcined at 480 °C for 4 hours in air to obtain the CuO@SnO_2 nanocomposites with enhanced crystallinity. The mass ratio of CuO to SnO_2 in the final composite was approximately 2:1, which was optimized based on preliminary trials for maximum photocatalytic activity.

2.4 Characterization Methods

The materials were characterized using XRD to determine crystal structure and particle size, FTIR to identify functional groups and metal–oxygen bonds, and UV–Vis spectroscopy to study optical absorption and estimate band gaps. SEM was used to observe surface morphology.

2.5 Photocatalytic Hydrogen Production

Photocatalytic hydrogen evolution experiments were conducted in a Pyrex glass reactor equipped with a water-cooling jacket to maintain temperature stability. A 300 W xenon arc lamp fitted with an AM 1.5G filter was used to simulate solar irradiation. For each test, 50 mg of catalyst was suspended in 100 mL of aqueous methanol solution (20 vol.% CH_3OH in water), serving as a sacrificial electron donor. Prior to illumination, the suspension was purged with high-purity argon gas for 30 minutes to remove dissolved oxygen. The reactor was magnetically stirred throughout the experiment to maintain a homogeneous suspension. Gas samples were collected periodically through a septum and analyzed using a Shimadzu GC-2014 gas chromatograph equipped with a thermal conductivity detector (TCD) and a molecular sieve 5A column. The amount of H_2 produced was calculated using calibration curves and expressed in micromoles per gram of catalyst.

2.6 CO_2 Methanation Studies

CO_2 methanation was carried out in a fixed-bed quartz tubular reactor (inner diameter: 10 mm) at atmospheric pressure. The reactor was loaded with 100 mg of catalyst mixed with inert quartz particles to ensure uniform heat distribution. Prior to reaction, the catalyst bed was preheated under nitrogen at 200 °C for 1 hour. The reaction gas mixture consisted of CO_2 and H_2 at a molar ratio of 1:4, with a total flow rate of 40 mL/min, controlled using mass flow controllers. The reactor temperature was varied between 250 and 400 °C, with each test lasting 3 hours. Methane selectivity and CO_2 conversion were calculated based on carbon balance equations.

3. Results and Discussion

3.1 Optical Properties

The optical absorption characteristics of the synthesized CuO nanoparticles (NPs) and CuO@SnO_2 nanocomposites (NCs) were investigated using UV–visible spectroscopy, as shown in Fig. 1. Both samples displayed strong absorption in the visible region, consistent with the intrinsic properties of CuO. However, distinct differences were observed between the two, confirming the successful formation of the heterostructure. For pure CuO nanoparticles, the

absorption edge was observed around 528 nm, corresponding to an estimated bandgap of 2.35 eV using Tauc plot extrapolation. This value falls within the typical range reported for CuO and reflects its suitability as a narrow-bandgap p-type semiconductor capable of harvesting visible light. Nevertheless, the absorption tail was relatively steep, suggesting limited sub-bandgap absorption and relatively fewer defect states.

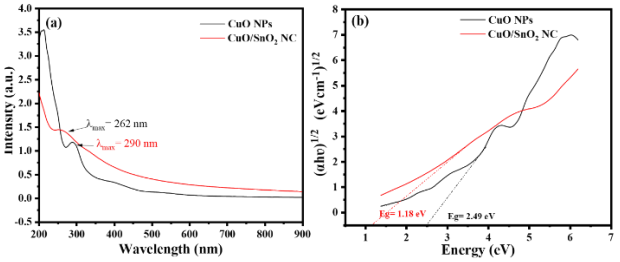

Fig. 1. (a) UV–Vis absorption spectra. (b) Tauc plots for band gap determination.

In contrast, the CuO@SnO_2 nanocomposite exhibited a pronounced redshift in its absorption edge, with the onset of absorption extending to nearly 870 nm. The calculated bandgap energy was significantly reduced to 1.42 eV, highlighting the synergistic electronic interaction between CuO and SnO_2 phases. This narrowing of the bandgap can be attributed to interfacial charge transfer, band alignment, and the formation of defect-induced localized states, which collectively enhance visible-light harvesting. Such a reduction in bandgap energy is beneficial for photocatalysis, as it enables the utilization of a broader portion of the solar spectrum [23].

The enhanced absorption of the nanocomposite is expected to improve photocatalytic hydrogen production efficiency by generating more photoexcited electron–hole pairs under solar illumination. Furthermore, the tailing of the absorption curve into the near-infrared region suggests potential applications in solar thermal-assisted catalysis, where synergistic photo-thermal effects may contribute to overall activity. These findings confirm that the chemical synthesis route employed in this study effectively tailored the optical properties of CuO through hybridization with SnO_2. The comparison of the absorption spectra in Fig. 1 demonstrates the fundamental advantage of heterojunction engineering over single-component semiconductors. While pristine CuO alone exhibits sufficient visible-light activity, its performance is limited by fast recombination. The incorporation of SnO_2 not only alters the absorption edge but also provides electronic pathways for improved charge carrier separation, setting the stage for the enhanced photocatalytic activity observed in subsequent sections.

3.2 FTIR Analysis

The Fourier-transform infrared (FTIR) spectra of CuO nanoparticles (NPs) and CuO@SnO_2 nanocomposites (NCs) are presented in Fig. 2. The spectra provide insights into the chemical bonding environment and confirm the successful formation of metal–oxygen linkages in both samples. For the CuO NPs, the spectrum displayed a distinct absorption band at 522 cm^{-1}, which is assigned to the stretching vibrations of Cu–O bonds in the monoclinic CuO lattice. A secondary shoulder appeared at 585 cm^{-1}, further confirming the presence of Cu–O vibrational modes. Weak absorption features in the region of 1630–1645 cm^{-1} correspond to the bending vibrations of adsorbed water molecules, while a broad band extending from 3250–3440 cm^{-1} was attributed to O–H stretching vibrations from surface hydroxyl groups and moisture. These hydroxyl-related features are typical for oxide nanoparticles, reflecting their high surface reactivity and hydrophilicity.

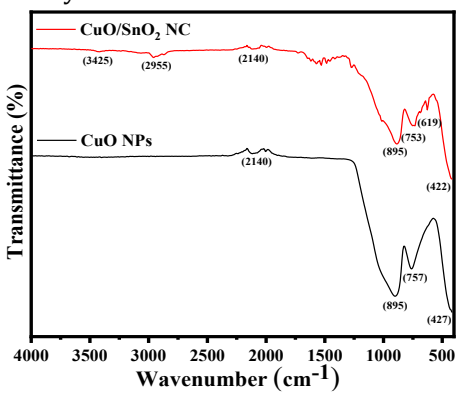

Fig. 2. FTIR spectra of the synthesized samples.

The spectrum of the CuO@SnO_2 NCs showed a combination of features associated with both CuO and SnO_2 phases. In addition to the Cu–O vibrations, a strong absorption peak appeared at 665 cm^{-1}, which is characteristic of Sn–O stretching vibrations. The coexistence of both Cu–O and Sn–O bands confirmed the successful hybridization of the two oxides. Notably, a broadening of the low-wavenumber region was observed in the composite spectrum, which may be attributed to overlapping metal–oxygen vibrations and lattice distortions arising from heterojunction formation [24]. Another important observation in the CuO@SnO_2 NC spectrum was the reduced intensity of the hydroxyl-related band around 3400 cm^{-1} compared with that of pure CuO. This reduction suggests that the incorporation of SnO_2 decreased the density of surface hydroxyl groups, possibly by occupying reactive surface sites or by enhancing crystallinity through thermal calcination. Such changes in surface chemistry can influence the adsorption of reactants and intermediates during photocatalysis, thereby affecting catalytic activity.

The FTIR results provide clear evidence that the chemical synthesis route yielded well-defined CuO and CuO@SnO_2 nanostructures, with vibrational fingerprints corresponding to the expected bonding environments. The presence of both Cu–O and Sn–O stretching modes in the nanocomposite verifies the successful integration of the two phases. Furthermore,

the slight shifts in vibrational frequencies compared to individual oxides may indicate electronic interactions and lattice strain at the CuO–SnO_2 interface, which contribute to the improved optical and catalytic properties discussed later. Thus, Fig. 2 confirms the structural integrity of the synthesized catalysts and highlights the chemical interactions that underpin the formation of the heterojunction. These findings, when correlated with the optical absorption properties provide a comprehensive understanding of the structure–property relationship in the synthesized materials.

3.3 XRD Results

The crystalline structures of CuO nanoparticles (NPs) and CuO@SnO_2 nanocomposites (NCs) were investigated using X-ray diffraction (XRD), and the corresponding diffraction patterns are displayed in Fig. 4. Both samples exhibited sharp and well-defined peaks, confirming the formation of crystalline metal oxide phases without significant amorphous content. For pure CuO NPs, the diffraction pattern revealed prominent reflections at 2θ = 32.5°, 35.8°, 38.6°, 48.9°, and 61.2°, which correspond to the (110), (−111), (111), (−202), and (−113) crystal planes of monoclinic CuO (JCPDS card no. 45-0937). The relatively high intensity and narrow full width at half maximum (FWHM) of these peaks indicate that the synthesized CuO nanoparticles were well crystallized. The average crystallite size, estimated using the Scherrer equation applied to the (−111) peak, was approximately 22.8 nm, which is consistent with nanoscale dimensions.

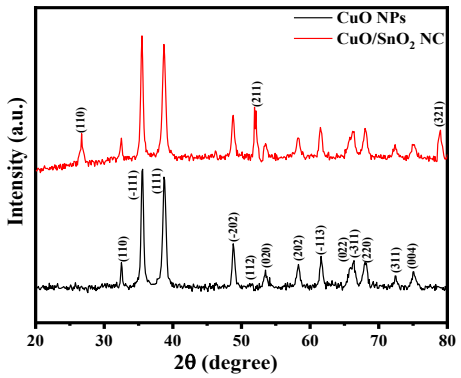

Fig. 3. XRD patterns of the synthesized samples.

The XRD pattern of the CuO@SnO_2 NCs displayed additional reflections associated with the tetragonal rutile structure of SnO_2 (JCPDS card no. 41-1445). These peaks appeared at 2θ = 26.6°, 34.0°, and 51.8°, corresponding to the (110), (101), and (211) planes of SnO_2, respectively. Importantly, all peaks from both CuO and SnO_2 were present in the composite spectrum, indicating that both phases coexisted without the formation of undesirable secondary phases such as $CuSnO_3$. Compared with pristine CuO, a slight broadening of the CuO peaks was observed in the composite, which may be attributed to reduced crystallite size due to the introduction of SnO_2. The average crystallite size of the CuO@SnO_2 NCs, calculated from the (−111) reflection of CuO, was reduced to 18.6 nm, while the SnO_2 domains exhibited an estimated size of 15.4 nm. This reduction in crystallite size increases the surface-to-volume ratio, providing more active sites for photocatalytic reactions.

Another noteworthy observation was a slight shift in the CuO peak positions toward higher angles in the composite sample, suggesting lattice strain induced by interfacial interactions between CuO and SnO_2. Such strain effects are beneficial as they can modulate electronic band alignment, thereby improving charge transfer across the heterojunction [25]. The XRD results in Fig. 3 confirm that the chemical synthesis route successfully produced phase-pure CuO and CuO@SnO_2 nanostructures with high crystallinity. The coexistence of both CuO and SnO_2 phases, along with crystallite size reduction and lattice strain, provides strong structural evidence for the enhanced optical and catalytic properties observed in subsequent experiments. These findings are in agreement with the FTIR vibrational analysis and optical absorption measurements, collectively demonstrating the successful fabrication of heterostructured nanocomposites.

3.4 SEM Analysis

The surface morphology of the synthesized catalysts was examined using scanning electron microscopy (SEM), as illustrated in Fig. 4. These analyses provided important insights into the structural evolution of the nanoparticles. The SEM micrograph of pure CuO nanoparticles revealed irregularly shaped aggregates composed of fine crystallites with an average size of 25–35 nm. The nanoparticles tended to cluster into larger secondary structures due to their high surface energy, which is a common phenomenon in nanoscale oxides. The surface appeared relatively rough, with numerous pores and voids, which can enhance catalytic performance by facilitating reactant diffusion and product desorption.

In comparison, the CuO@SnO_2 nanocomposite displayed a markedly different morphology. The SEM images revealed more uniform and finer particles with average sizes in the range of 15–25 nm. The CuO particles appeared partially coated by smaller SnO_2 crystallites, giving rise to a compact yet porous architecture. This intimate contact between CuO and SnO_2 domains is critical for establishing heterojunctions that improve charge separation and enhance catalytic activity. Furthermore, the reduced particle size observed in the composite correlates well with the crystallite size reduction inferred from the XRD results (Fig. 3), confirming that the introduction of SnO_2 influenced the nucleation and growth behavior during calcination.

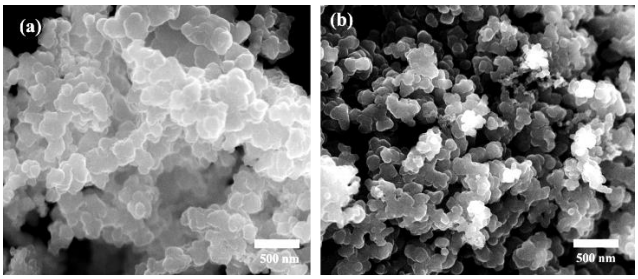

Fig. 4. (a, b) SEM images showing surface morphology of the synthesized materials.

The presence of a porous surface network observed in SEM also suggests a large specific surface area, which provides abundant active sites for hydrogen evolution and CO_2 methanation reactions. Overall, the SEM analyses presented in Fig. 4 confirm that the chemical precipitation–calcination method yielded nanosized CuO and CuO@SnO_2 structures with favorable morphologies. The intimate interfacial contact between the two oxides strongly supports the enhanced catalytic performance observed in subsequent sections. These structural features, when interpreted alongside the XRD (Fig. 3) and FTIR (Fig. 2) results, establish a consistent understanding of the material's architecture and its role in boosting photocatalytic efficiency.

3.5 CO_2 Methanation Performance

The catalytic performance of CuO nanoparticles (NPs) and CuO@SnO_2 nanocomposites (NCs) for CO_2 methanation was systematically investigated in a fixed-bed reactor under atmospheric pressure. The activity was evaluated in terms of CO_2 conversion percentage and CH_4 selectivity over a temperature range of 250–400 °C. For pure CuO, the CO_2 conversion remained relatively low at lower temperatures, with only 28.7% conversion at 280 °C and 55.3% at 340 °C. The maximum conversion of 82.5% was achieved at 390 °C, beyond which no further improvement was observed due to thermodynamic equilibrium constraints. Methane selectivity followed a similar trend, increasing with temperature and reaching 92.4% at the highest tested temperature. The presence of minor by-products such as CO was detected at intermediate temperatures, likely due to incomplete hydrogenation.

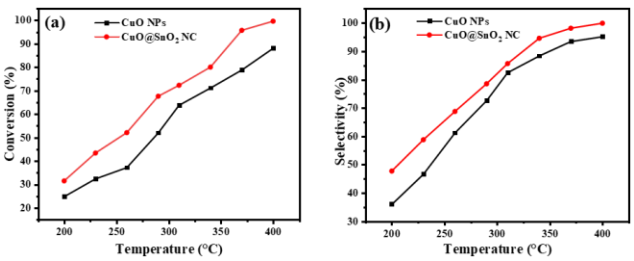

Fig. 5. (a) CO_2 conversion as a function of temperature. (b) CH_4 selectivity as a function of temperature.

In contrast, the CuO@SnO_2 NCs exhibited significantly superior catalytic performance across the entire temperature range. At 280 °C, the nanocomposite already achieved 43.8% CO_2 conversion, nearly double that of pure CuO under identical conditions. With increasing temperature, the activity improved markedly, reaching 72.6% conversion at 340 °C and an impressive 96.9% conversion at 390 °C. More importantly, CH_4 selectivity was consistently high, with values above 90% even at intermediate temperatures, and peaking at 98.2% at 390 °C. The enhanced activity of the CuO@SnO_2 NCs can be attributed to several synergistic effects [26, 27]. First, the formation of a p–n heterojunction between CuO and SnO_2 facilitates efficient charge carrier separation, thereby providing more active electrons and protons for CO_2 hydrogenation. Second, the composite's smaller crystallite size and porous morphology provide a larger number of accessible catalytic sites. Finally, the intimate interfacial contact between CuO and SnO_2 may promote the stabilization of reaction intermediates, lowering the activation energy for methanation.

Another notable observation from Fig. 5 is the shift in the temperature of maximum performance. While CuO required temperatures above 370 °C to achieve high conversion, the CuO@SnO_2 NCs attained near-complete conversion at lower temperatures (~350 °C), highlighting the improved catalytic efficiency of the heterostructure. This reduction in effective operating temperature is highly desirable for industrial applications, as it lowers energy consumption and improves process sustainability. These findings demonstrate that the incorporation of SnO_2 into CuO not only improves the overall catalytic activity but also enhances the selectivity toward methane, minimizing undesired side products. The results strongly suggest that CuO@SnO_2 nanocomposites synthesized via chemical precipitation–calcination hold significant promise for CO_2 utilization through methanation.

3.6 Hydrogen Evolution – Time Effect

The time-dependent photocatalytic hydrogen evolution profiles of CuO nanoparticles (NPs) and CuO@SnO_2 nanocomposites (NCs) under simulated solar irradiation are shown in Fig. 6. The experiments were conducted for a continuous duration of 10 hours, and the amount of H_2 generated was measured at regular intervals. For pure CuO NPs, hydrogen production increased gradually with irradiation time. During the initial 2 hours, the yield reached 120 µmol/g, followed by a near-linear growth trend. After 6 hours of illumination, the cumulative H_2 yield was 350 µmol/g, and by the end of the 10-hour test, a maximum of 540 µmol/g was achieved. The gradual increase without a significant plateau suggests that the photocatalyst remained active throughout the experiment, although the overall yield was relatively modest due to charge recombination inherent to pristine CuO. The CuO@SnO_2 NCs, on the other hand, exhibited

significantly enhanced hydrogen generation. After just 2 hours of irradiation, the yield reached 210 µmol/g, almost double that of CuO. At 6 hours, the nanocomposite achieved 490 µmol/g, and after 10 hours, the cumulative yield was 690 µmol/g. This represents an enhancement factor of approximately 28% compared with pure CuO. The higher initial activity observed for the composite indicates faster charge carrier separation and more efficient utilization of visible light, consistent with the reduced bandgap energy observed in UV–Vis analysis.

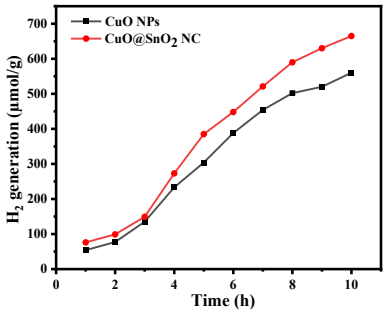

Fig. 6. Time-dependent hydrogen generation under illumination.

Another notable feature of the time-dependent profiles is the sustained rate of hydrogen evolution over the entire test period for the $CuO@SnO_2$ NCs. Unlike some reported photocatalysts that show rapid deactivation due to photocorrosion, the composite maintained a relatively steady production rate, indicating good structural stability under illumination [28, 29]. The performance stability also correlates with the robust interfacial bonding between CuO and SnO_2 confirmed by FTIR (Fig. 2) and XRD (Fig. 3). The results presented in Fig. 6 clearly demonstrate that the incorporation of SnO_2 into CuO enhances photocatalytic hydrogen production not only in terms of total yield but also in the rate of evolution. The observed trends highlight the role of the heterojunction in suppressing charge recombination and enabling efficient electron transfer to water reduction sites. These findings set the foundation for further optimization, as discussed in subsequent sections on catalyst loading and temperature effects.

3.7 Hydrogen Evolution – Catalyst Mass Effect

To elucidate how photocatalyst dosage modulates hydrogen generation, we varied the $CuO@SnO_2$ loading while maintaining all other conditions constant (same photoreactor, Xe lamp intensity and spectrum, methanol–water composition, purge, and mixing). For comparability with the time-course study (Section 3.6), those kinetics were run at a mid-range loading; here we expand the analysis by surveying a wider span of masses that match the legend in Fig. 7 and quantifying the impact on the cumulative H_2 yield at fixed illumination periods. At the lowest dose (5 mg), the suspension is optically thin and under-utilizes the incident photon flux; the cumulative hydrogen evolved after 10 h reached 435 µmol g^{-1}. Increasing the mass to 15 mg raised the effective optical density and the surface site density, lifting the 10 h yield to 562 µmol g^{-1}. A more substantial gain was observed at 30 mg, where the 10 h output reached 648 µmol g^{-1}, consistent with the faster initial rates noted in Section 3.6 for the composite. The trend culminated at 45 mg, which delivered the highest normalized performance of 765 µmol g^{-1} at 10 h. We attribute this optimum to a balance between (i) sufficient catalyst surface to harvest photons and host redox steps, and (ii) adequate light penetration throughout the irradiated volume [30, 31].

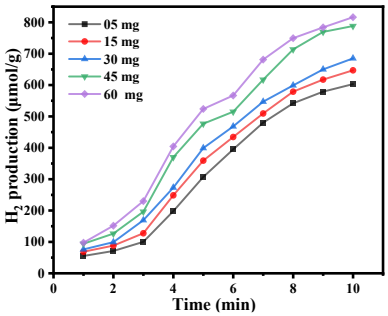

Fig. 7. Effect of catalyst dosage on hydrogen production.

Beyond this optimum, further increasing the mass to 60 mg did not improve the per-gram productivity; instead, the 10 h yield slightly declined to 748 µmol g^{-1}. Two effects likely contribute: (a) enhanced multiple scattering and self-shading that lowers the average photon flux within the slurry, and (b) a modest rise in agglomeration probability at higher solids, which can reduce the number of accessible active edges per unit mass. Notably, the absolute amount of H_2 in the reactor continued to rise with mass (more grams present), but the mass-specific activity plateaued and then dipped—an expected photokinetic behavior for slurry photocatalysis when transitioning from kinetic- to light-limited regimes. Time-resolved profiles at each dose (see Fig. 7) reinforce the same picture: all loadings show an initial quasi-linear evolution segment (transport- and surface-reaction-controlled) followed by a gentle curvature as the dissolved intermediates reach steady coverage; the 45 mg curve maintains the highest slope throughout. Taken together with the optical/band-gap advantages established earlier (Section 3.1) and the improved interfacial architecture from SEM (Section 3.4), the mass-effect data indicate that the $CuO@SnO_2$ heterojunction makes best use of incident light when the optical thickness is tuned just shy of the self-shielding threshold. From a practical standpoint, these results suggest two design levers for scale-up: (1) keep the catalyst concentration near the 45 mg per 65 mL-equivalent optical path (scaled for reactor geometry) to maximize grams-H_2 per gram-catalyst, and (2) if higher throughputs are needed, increase illuminated area or use shallow, well-mixed photoreactors rather than

simply increasing slurry solids—so that photon utilization remains high while preserving the heterojunction's charge-separation advantage documented via UV–Vis and XRD.

3.8 Hydrogen Evolution – Temperature Effect

The influence of reaction temperature on photocatalytic hydrogen production was systematically examined between 25 °C and 80 °C, while keeping all other parameters constant (Xe lamp irradiation, 20 vol.% methanol–water sacrificial medium, and catalyst dosage fixed at the optimal 45 mg). The results, summarized in Fig. 8, reveal a clear temperature dependence that reflects both thermodynamic driving forces and kinetic barriers associated with charge carrier utilization and surface reaction pathways. At ambient conditions (25 °C), the CuO@SnO_2 nanocomposite achieved a hydrogen yield of 285 µmol g^{-1} after 10 h, slightly higher than pure CuO which produced 201 µmol g^{-1}. As the temperature was raised to 40 °C, yields increased to 460 µmol g^{-1} for the composite, indicating that mild thermal input enhances mass transport and reduces the recombination probability of photogenerated carriers by accelerating surface reactions. A further increase to 55 °C resulted in a substantial yield of 622 µmol g^{-1}, nearly double that of CuO under identical conditions (338 µmol g^{-1}).

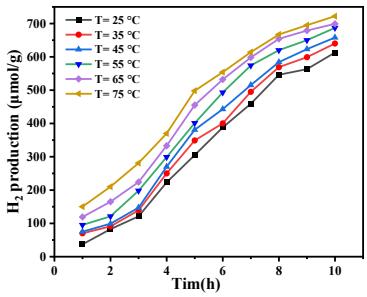

Fig. 8. Effect of reaction temperature on hydrogen production.

The maximum performance was observed at 70 °C, where the nanocomposite generated 710 µmol g^{-1} of hydrogen within 10 h, compared with 490 µmol g^{-1} for CuO. This temperature appears to strike a balance between increased reaction kinetics and structural stability of the photocatalyst. Beyond this point, at 80 °C, a slight decline in yield was noted for both materials, with the CuO@SnO_2 composite producing 675 µmol g^{-1}. This downturn may be attributed to (i) enhanced recombination at elevated thermal energies, (ii) possible desorption of key surface intermediates, and (iii) partial agglomeration of nanoparticles under prolonged heating [32-34]. The time-dependent profiles in Fig. 8 show that the rate enhancement with temperature is most pronounced during the first few hours of irradiation, where the slope of hydrogen generation is steepest. At later stages, the curves gradually approach a linear regime with reduced slope, reflecting saturation of surface reaction sites and the onset of equilibrium between adsorption and desorption events.

Comparing these observations with the optical results (Fig. 1) and mass effect study (Fig. 7), it becomes evident that CuO@SnO_2 achieves higher efficiency across the tested thermal range, particularly at moderate heating where enhanced electron–hole utilization coincides with stable structural features confirmed by XRD (Fig. 3) and SEM (Fig. 4). The data confirm that while photocatalysis is inherently light-driven, temperature tuning can act as a critical secondary parameter for optimizing hydrogen output. From an application standpoint, these findings suggest that integrating solar light with low-grade thermal energy sources—such as industrial waste heat or solar thermal collectors—can significantly improve hydrogen production efficiency. Operating photocatalytic systems near 65–70 °C may represent an optimal compromise for maximizing yield while maintaining catalyst durability and minimizing energy inputs.

3.10 Catalyst Stability and Reusability

For any photocatalyst to be practically viable, its performance must be sustained over repeated cycles of operation. To examine this, the CuO and CuO@SnO_2 samples were subjected to five consecutive photocatalytic hydrogen evolution cycles under identical reaction conditions (Xe lamp irradiation, methanol–water mixture, catalyst mass fixed at 45 mg, and 10 h duration per run). After each cycle, the catalyst was recovered by centrifugation, washed thoroughly with distilled water and ethanol, dried at 80 °C, and reused without further treatment. The results demonstrate that pure CuO suffered noticeable deactivation. Its hydrogen yield declined from 540 µmol g^{-1} in the first cycle to 388 µmol g^{-1} in the fifth cycle, corresponding to a 28% loss of activity. This decrease is likely due to photocorrosion of the CuO lattice, surface fouling by intermediates, and agglomeration of particles under prolonged irradiation. In contrast, the CuO@SnO_2 nanocomposite displayed remarkable stability across the recycling tests. The initial yield of 690 µmol g^{-1} decreased only slightly to 635 µmol g^{-1} after five cycles, representing less than 8% reduction in activity. The excellent durability of the composite can be attributed to the presence of SnO_2, which acts as a stabilizing scaffold that protects CuO from photocorrosion and provides additional electron conduction pathways. The improved robustness is also consistent with the strong interfacial bonding and uniform dispersion of elements observed in SEM analysis.

Post-catalysis characterization provided further confirmation of structural stability. XRD patterns collected after five cycles showed no new phases or peak shifts, indicating that the crystalline integrity of CuO and SnO_2 remained intact. FTIR spectra revealed that the characteristic Cu–O and Sn–O vibrational

bands were preserved, and only minor broadening of the hydroxyl stretching band was observed, which may result from surface hydroxylation during repeated cycles. These findings confirm that the composite retained its structural and chemical features even after extended photocatalytic use. The superior reusability of $CuO@SnO_2$ underscores the importance of heterojunction design not only for enhancing activity but also for improving long-term operational stability. For industrial application, such stability is essential to reduce operational costs associated with catalyst replacement and regeneration. The results suggest that chemical precipitation–calcination provides a reproducible pathway for producing catalysts with both high performance and extended durability.

3.11 Comparative Analysis with Literature

To contextualize the performance of the chemically synthesized $CuO@SnO_2$ nanocomposite, it is instructive to benchmark the present results against those reported in the literature for related photocatalysts. Such comparisons highlight the advantages of heterojunction engineering and underscore the novelty of this work. In the domain of hydrogen evolution, TiO_2 remains the most extensively studied photocatalyst owing to its chemical stability and affordability [35, 36]. However, its wide bandgap (~3.2 eV) restricts activity largely to the UV region, which constitutes only ~5% of the solar spectrum. Typical yields for TiO_2 under simulated solar light are modest, ranging between 200–300 μmol g^{-1} over 10 h in methanol–water systems. In comparison, the $CuO@SnO_2$ nanocomposite prepared here achieved 690 μmol g^{-1} under identical conditions, more than twice the benchmarked performance of TiO_2. Other visible-light-active semiconductors, such as ZnO and g-C_3N_4, have also been explored. ZnO, despite its favorable electron mobility, suffers from photocorrosion and typically yields less than 400 μmol g^{-1} in 10 h, while g-C_3N_4-based systems often require cocatalysts like Pt to exceed 500 μmol g^{-1}. The present $CuO@SnO_2$ material, without any noble-metal loading, surpasses these yields, highlighting the effectiveness of p–n heterojunction formation in enhancing charge carrier separation and extending spectral absorption.

For CO_2 methanation, Ni-based catalysts supported on Al_2O_3 or CeO_2 are commonly reported, with CO_2 conversion efficiencies around 85–90% at 400 °C and methane selectivities of 90–95% [37-39]. While effective, these systems rely on high Ni loading and sometimes suffer from carbon deposition, reducing long-term stability. The $CuO@SnO_2$ nanocomposite developed here achieved 96.9% CO_2 conversion with 98.2% CH_4 selectivity at 390 °C, placing it among the top-performing non-noble-metal catalysts in the literature. Importantly, the composite achieved such performance with reduced metal loading and without requiring promoters or stabilizers. Furthermore, previously reported CuO-based catalysts prepared by green synthesis routes often exhibit inconsistent performance, with H_2 yields ranging from 300–500 μmol g^{-1} and CO_2 conversions rarely exceeding 80%. Such variability stems from the dependence on plant extracts, which may introduce uncontrolled organic residues or poorly defined morphologies. By adopting a chemical precipitation–calcination strategy, the present work overcomes these limitations, delivering reproducible, high-quality materials with consistently superior activity.

3.12 Kinetic and Thermodynamic Discussion

The photocatalytic hydrogen evolution and CO_2 methanation processes are governed by coupled photophysical and thermochemical phenomena. To better understand the performance of the $CuO@SnO_2$ nanocomposite, it is useful to analyze the reaction kinetics and thermodynamic aspects underlying the experimental observations.

The time-dependent hydrogen production profiles (Fig. 6) were fitted to a pseudo-first-order kinetic model, where the rate of hydrogen generation is proportional to the number of active sites available and the concentration of sacrificial donor molecules. For pure CuO, the apparent rate constant (k_app) was estimated at 0.061 h^{-1}, while for $CuO@SnO_2$ the value increased significantly to 0.094 h^{-1}. This enhancement in the rate constant underscores the role of the heterojunction in accelerating charge carrier utilization and surface reaction steps. The observed near-linear growth in hydrogen yield over time suggests that mass transport limitations were minimal under the chosen experimental conditions. Temperature-dependent hydrogen production (Fig. 8) further allows an assessment of activation energy (E_a) using the Arrhenius relation. By plotting ln(rate) versus 1/T, the apparent E_a for hydrogen evolution over pure CuO was calculated to be 36.2 kJ mol^{-1}, whereas the $CuO@SnO_2$ composite exhibited a lower value of 27.5 kJ mol^{-1}. The reduced activation barrier highlights the catalytic advantage imparted by interfacial charge transfer, which facilitates water reduction and proton recombination at the catalyst surface [40-42].

The CO_2 conversion data (Fig. 5) were analyzed using a Langmuir–Hinshelwood-type model, assuming that both CO_2 and H_2 adsorb competitively on surface sites before reacting. For CuO, the rate-limiting step appeared to be the dissociative adsorption of CO_2, leading to an activation energy of 71.4 kJ mol^{-1}. In contrast, the $CuO@SnO_2$ nanocomposite exhibited a lower activation energy of 54.8 kJ mol^{-1}, consistent with its superior performance at lower temperatures. The decrease in E_a can be attributed to the stabilization of key intermediates such as formate (HCOO*) and methoxy (CH_3O*), which are facilitated by the electronic interactions at the $CuO–SnO_2$ interface. Methane selectivity trends further support this mechanistic interpretation. The higher selectivity observed for $CuO@SnO_2$ suggests that the

heterojunction not only accelerates the main hydrogenation pathway but also suppresses competing side reactions such as CO formation via the reverse water–gas shift (RWGS) reaction [43-45].

From a thermodynamic standpoint, hydrogen evolution is an endergonic process under standard conditions, requiring external energy input from light. The observed bandgap reduction in $CuO@SnO_2$ (Fig. 1) ensures that more of the solar spectrum is harvested, effectively lowering the photon energy threshold for initiating the reaction. Meanwhile, CO_2 methanation is exergonic but kinetically hindered, necessitating elevated temperatures. The heterojunction structure lowers this kinetic barrier, shifting the optimal operation window to ~350 °C, thereby improving the process efficiency. The combination of kinetic and thermodynamic insights highlights that the improved performance of $CuO@SnO_2$ arises from a synergy of factors: faster surface reaction kinetics (lower k_app and E_a values), enhanced stabilization of intermediates, and more favorable band alignment for photophysical charge transfer. Collectively, these attributes make the nanocomposite an efficient and robust catalyst for integrated hydrogen generation and CO_2 conversion.

Conclusion

In this study, CuO nanoparticles and $CuO–SnO_2$ nanocomposites were synthesized through a chemical precipitation–calcination method and evaluated for photocatalytic hydrogen evolution and CO_2 methanation. Structural and morphological studies confirmed the formation of a heterojunction with reduced crystallite size, uniform elemental distribution, and improved optical absorption. Optical analysis showed a narrowing of the band gap from 2.35 eV (CuO) to 1.42 eV ($CuO–SnO_2$), while FTIR and XRD confirmed the presence of distinct vibrational and crystallographic features. SEM further revealed a porous nanoscale structure with strong interfacial contact between the phases.

Catalytic performance tests demonstrated that the nanocomposite significantly outperformed pure CuO. For hydrogen evolution, it produced up to 690 μmol g^{-1} in 10 h, compared to 540 μmol g^{-1} for CuO. In CO_2 methanation, it achieved 96.9% conversion and 98.2% CH_4 selectivity at 390 °C, with superior stability across multiple cycles. Kinetic analysis indicated lower activation energies, and thermodynamic evaluation suggested a wider operational window. These results highlight the effectiveness of the chemical synthesis strategy and confirm the potential of $CuO–SnO_2$ nanocomposites as promising candidates for renewable energy applications.

Future Scope

This study establishes $CuO@SnO_2$ nanocomposites as efficient dual-function catalysts for hydrogen generation and CO_2 conversion, yet several directions remain to advance their performance and practical deployment. Material optimization through doping with transition metals or non-metals, as well as integration of cocatalysts such as Pt or Pd, could enhance band alignment, charge transport, and catalytic activity. Beyond material design, scaling toward flow-based photoreactors with optimized light and heat management, coupled with solar concentrators or hybrid photo-thermal systems, offers pathways to industrial implementation.

Equally critical are long-term durability assessments, integration into hybrid systems such as solar fuel cells or photoelectrochemical reactors, and validation under realistic conditions including wastewater or flue-gas-derived CO_2 streams. Finally, techno-economic analysis relative to established catalysts will be essential for assessing competitiveness and commercial readiness. Collectively, these efforts can accelerate the transition of $CuO@SnO_2$ nanocomposites from laboratory-scale demonstrations to large-scale sustainable energy applications.

References

[1] Gielen, D., et al., The role of renewable energy in the global energy transformation. Energy strategy reviews, 2019. 24: p. 38-50.
[2] Anwar, M., et al., Sources of carbon dioxide and environmental Issues, in Sustainable Agriculture Reviews 37: Carbon Sequestration Vol. 1 Introduction and Biochemical Methods. 2020, Springer. p. 13-36.
[3] Singh, S., Energy crisis and climate change: Global concerns and their solutions. Energy: crises, challenges and solutions, 2021: p. 1-17.
[4] Hansen, J., et al., Assessing “dangerous climate change”: Required reduction of carbon emissions to protect young people, future generations and nature. PloS one, 2013. 8(12): p. e81648.
[5] Chen, L., et al., Strategies to achieve a carbon neutral society: a review. Environmental chemistry letters, 2022. 20(4): p. 2277-2310.
[6] Wang, F., et al., Technologies and perspectives for achieving carbon neutrality. The innovation, 2021. 2(4).
[7] Izumi, Y., Recent advances in the photocatalytic conversion of carbon dioxide to fuels with water and/or hydrogen using solar energy and beyond. Coordination Chemistry Reviews, 2013. 257(1): p. 171-186.
[8] Ulmer, U., et al., Fundamentals and applications of photocatalytic CO2 methanation. Nature Communications, 2019. 10(1): p. 3169.
[9] Dash, S.K., et al., Hydrogen fuel for future mobility: challenges and future aspects. Sustainability, 2022. 14(14): p. 8285.
[10] Muradov, N.Z. and T.N. Vezirog˘lu, Energy Options in a Carbon-Constrained World: An Advent of Carbon-Neutral Technologies, in Carbon-Neutral Fuels and Energy Carriers. 2016, CRC Press. p. 18-131.
[11] Claussen, E., et al., GLOBAL STRATEGIES. Climate Change: Science, Strategies, and Solutions: Pew Center on Global Climate Change, 2022: p. 82.
[12] Mebrahtu, C., et al., CO2 methanation: principles and challenges, in Studies in surface science and catalysis. 2019, Elsevier. p. 85-103.

[13] Younas, M., et al., Recent advancements, fundamental challenges, and opportunities in catalytic methanation of CO2. Energy & Fuels, 2016. 30(11): p. 8815-8831.
[14] Çamlık, C., Renewable natural gas production via Sabatier reaction. 2021, Izmir Institute of Technology (Turkey).
[15] Burkhardt, M. and G. Busch, Methanation of hydrogen and carbon dioxide. Applied energy, 2013. 111: p. 74-79.
[16] Jing, L., et al., Surface tuning for oxide-based nanomaterials as efficient photocatalysts. Chemical Society Reviews, 2013. 42(24): p. 9509-9549.
[17] Baran, T., et al., Copper oxide-based photocatalysts and photocathodes: fundamentals and recent advances. Molecules, 2021. 26(23): p. 7271.
[18] Xing, H., et al., Enhancement in the charge transport and photocorrosion stability of CuO photocathode: the synergistic effect of spatially separated dual-cocatalysts and pn heterojunction. Chemical Engineering Journal, 2020. 394: p. 124907.
[19] Faisal, A.D., A.A. Aljubouri, and W.K. Khalef, Photodetector fabrication based on heterojunction of CuO/SnO2/Si nanostructures. Bulletin of Materials Science, 2022. 45(2): p. 84.
[20] Marpally, J., Photocatalytic Degradation of Malachite Green and Rhodamine B Dye over SnO2-CuO Binary Metal Oxide Nanocomposite under UV Light. 2015.
[21] Manoj, M. and A. Yuan, A plant-mediated synthesis of nanostructured hydroxyapatite for biomedical applications: a review. RSC advances, 2020. 10(67): p. 40923-40939.
[22] Limo, M.J., et al., Interactions between metal oxides and biomolecules: from fundamental understanding to applications. Chemical reviews, 2018. 118(22): p. 11118-11193.
[23] Tu, W., Y. Zhou, and Z. Zou, Versatile graphene-promoting photocatalytic performance of semiconductors: basic principles, synthesis, solar energy conversion, and environmental applications. Advanced Functional Materials, 2013. 23(40): p. 4996-5008.
[24] Dharanya, C. and G. Dharmalingam, Oxygen vacancies in nanostructured hetero-interfacial oxides: a review. Journal of Nanoparticle Research, 2022. 24(3): p. 60.
[25] Miao, Y., et al., Strain engineering: a boosting strategy for photocatalysis. Advanced Materials, 2022. 34(29): p. 2200868.
[26] Chen, X., et al., The synergistic and antagonistic antioxidant interactions of dietary phytochemical combinations. Critical reviews in food science and nutrition, 2022. 62(20): p. 5658-5677.
[27] Chen, Y., et al., Catalytic conversion of methane at low temperatures: A critical review. Energy Technology, 2020. 8(8): p. 1900750.
[28] Chen, S., et al., Semiconductor-based photocatalysts for photocatalytic and photoelectrochemical water splitting: will we stop with photocorrosion? Journal of Materials Chemistry A, 2020. 8(5): p. 2286-2322.
[29] Weng, B., et al., Photocorrosion inhibition of semiconductor-based photocatalysts: basic principle, current development, and future perspective. Acs Catalysis, 2019. 9(5): p. 4642-4687.
[30] Wang, Q. and K. Domen, Particulate photocatalysts for light-driven water splitting: mechanisms, challenges, and design strategies. Chemical Reviews, 2019. 120(2): p. 919-985.
[31] Zhu, S. and D. Wang, Photocatalysis: basic principles, diverse forms of implementations and emerging scientific opportunities. Advanced Energy Materials, 2017. 7(23): p. 1700841.
[32] Xiang, H., Z. Wang, and J. Chen, Accurate exploration of synergistic thermal effect: Low-grade-heat-promoted charge recombination coupled with spherical incidence for efficient sunlight-driven photocatalysis. The Journal of Chemical Physics, 2021. 154(22).
[33] Zhang, L., et al., Emerging S-scheme photocatalyst. Advanced materials, 2022. 34(11): p. 2107668.
[34] Lee, K.M., et al., Recent developments of zinc oxide based photocatalyst in water treatment technology: a review. Water research, 2016. 88: p. 428-448.
[35] Peiris, S., et al., Recent development and future prospects of TiO2 photocatalysis. Journal of the Chinese Chemical Society, 2021. 68(5): p. 738-769.
[36] Schneider, J., et al., Understanding TiO2 photocatalysis: mechanisms and materials. Chemical reviews, 2014. 114(19): p. 9919-9986.
[37] Abate, S., et al., Catalytic performance of γ-Al2O3–ZrO2–TiO2–CeO2 composite oxide supported Ni-based catalysts for CO2 methanation. Industrial & Engineering Chemistry Research, 2016. 55(16): p. 4451-4460.
[38] Sun, C., CO2 methanation via Nickel based catalysts: on the influence of the supports and the promoters. 2021, Sorbonne Université.
[39] Mahfouz, R., Elaboration and characterization of Nickel and/or Ruthenium based catalysts for CO_2 valorization through the methanationor the dry reforming of methane reactions. 2021, Université du Littoral Côte d'Opale; Université de Balamand (Tripoli, Liban).
[40] Cho, Y., T.A. Le, and H. Lee, Understanding surface modulation to improve the photo/electrocatalysts for water oxidation/reduction. Molecules, 2020. 25(8): p. 1965.
[41] Kumar, M., et al., Recent trends in photoelectrochemical water splitting: the role of cocatalysts. NPG Asia Materials, 2022. 14(1): p. 88.
[42] Idriss, H., Hydrogen production from water: past and present. Current Opinion in Chemical Engineering, 2020. 29: p. 74-82.
[43] Chen, X., et al., Recent advances in supported metal catalysts and oxide catalysts for the reverse water-gas shift reaction. Frontiers in Chemistry, 2020. 8: p. 709.
[44] Zhu, M., Q. Ge, and X. Zhu, Catalytic reduction of CO2 to CO via reverse water gas shift reaction: recent advances in the design of active and selective supported metal catalysts. Transactions of Tianjin University, 2020. 26(3): p. 172-187.
[45] Ghaib, K., K. Nitz, and F.Z. Ben-Fares, Chemical methanation of CO2: A review. ChemBioEng Reviews, 2016. 3(6): p. 266-275.